

# Fast Nonconvex $T_2^*$ Mapping Using ADMM

Shuai Huang, James J. Lah, Jason W. Allen and Deqiang Qiu

**Abstract**—Magnetic resonance (MR)- $T_2^*$  mapping is widely used to study hemorrhage, calcification and iron deposition in various clinical applications, it provides a direct and precise mapping of desired contrast in the tissue. However, the long acquisition time required by conventional 3D high-resolution  $T_2^*$  mapping method causes discomfort to patients and introduces motion artifacts to reconstructed images, which limits its wider applicability. In this paper we address this issue by performing  $T_2^*$  mapping from undersampled data using compressive sensing (CS). We formulate the reconstruction as a nonconvex problem that can be decomposed into two subproblems. They can be solved either separately via the standard approach or jointly via the alternating direction method of multipliers (ADMM). Compared to previous CS-based approaches that only apply sparse regularization on the spin density  $X_0$  and the relaxation rate  $R_2^*$ , our formulation enforces additional sparse priors on the  $T_2^*$ -weighted images at multiple echoes to improve the reconstruction performance. We performed convergence analysis of the proposed algorithm, evaluated its performance on *in vivo* data, and studied the effects of different sampling schemes. Experimental results showed that the proposed joint-recovery approach generally outperforms the state-of-the-art method, especially in the low-sampling rate regime, making it a preferred choice to perform fast 3D  $T_2^*$  mapping in practice. The framework adopted in this work can be easily extended to other problems arising from MR or other imaging modalities with non-linearly coupled variables.

**Index Terms**—Quantitative MRI,  $T_2^*$  mapping,  $T_2$  mapping, compressive sensing, ADMM

## I. INTRODUCTION

Conventional magnetic resonance (MR) imaging techniques such as  $T_1$ -weighted,  $T_2$ -weighted imaging are not quantitative, and the produced images cannot be directly compared across different acquisition protocols or scanners. There has since been increasing interest in developing quantitative MR methods that directly measure properties such as spin density, longitudinal and transverse relaxation rates. Here we focus on studying the  $T_2^*$  relaxation process that is useful in a number of clinical applications [1]–[7]. Apart from the typical spin-spin relaxation (i.e.  $T_2$  relaxation),  $T_2^*$  relaxation also takes into account the transverse magnetization decay caused by magnetic field inhomogeneity. As a result,  $T_2^*$  is shorter than  $T_2$ , and they are connected by the following relationship [8]

$$\frac{1}{T_2^*} = \frac{1}{T_2} + \frac{1}{T_{2in}}, \quad (1)$$

where  $1/T_{2in} = \gamma \Delta B_{in}$ ,  $\gamma$  is the gyromagnetic ratio,  $\Delta B_{in}$  is the magnetic field inhomogeneity caused by magnetic

susceptibility differences within the tissues, chemical shift, and gradient fields applied for spatial encoding [9]. In order to preserve the inhomogeneity  $\Delta B_{in}$ , we use the gradient-echo (GRE) sequence to acquire the data. No  $180^\circ$  refocusing pulse is applied after the radio-frequency (RF) excitation, and measurements are acquired at multiple echo times (TE) within one repetition time (TR).

The tissue contrasts revealed by  $T_2^*$ -weighted images have proved quite useful in studying hemorrhage [1]–[3], calcification [4], [5], and iron deposition [6], [7] in various tissues and diseases. However, the *qualitative* contrast information obtained from a series of  $T_2^*$ -weighted images depends on the sampling pulse sequence and imaging platform. Furthermore, qualitative  $T_2^*$  image interpretation is subjective and may vary between readers. As a result, *quantitative* measurement of the  $T_2^*$  relaxation values has attracted a lot of interests in recent years, since it provides a direct and precise mapping of desired contrast in the tissue [10].  $T_2^*$  mapping has been used in a variety of clinical applications such as susceptibility-weighted imaging [11], [12], perfusion MR imaging [13], [14], functional MR imaging [15], [16] and iron overload imaging [17], [18]. In particular, the quantitative nature of  $T_2^*$  mapping has made it possible to detect and monitor small pathological changes in Alzheimer’s disease (AD) [19], [20]. An animal study [21] has shown that  $T_2^*$  relaxation values in the tissue are sensitive to early changes in Tau pathology, a key neuropathological hallmark of AD. This could provide valuable biomarker information in helping the clinicians to predict risk of transition from normal cognition to mild cognitive impairment (MCI), and the rate of deterioration in MCI patients.

Three-dimensional (3D) high-resolution imaging is usually needed to find early predictive biomarkers of diseases such as AD, so that early pathological changes could be localized within small anatomical structures [22]. High-resolution  $T_2^*$  mapping has also been found to be useful in studying iron loading in Parkinson’s Disease [23], [24], as well as in the quantification of the liver overloading [25], [26]. The long acquisition time required by conventional  $T_2^*$  mapping methods causes discomfort to the patients, introduces motion artifacts to the reconstructed images, and reduces the throughput of clinical imaging studies. Developing fast imaging methods that operate at lower sampling rates to reduce the scan time is thus of great importance in practice. In this paper we use compressive sensing (CS) techniques [27], [28] to perform  $T_2^*$  mapping from undersampled data. We formulate the reconstruction into the following two subproblems:

- 1) Reconstruction of the magnitude images  $X_i$  and the phase images  $Z_i$  at multiple echo times  $i \in \{1, \dots, E\}$ .

This work is supported by National Institutes of Health under Grants R21AG064405 and P50AG025688. (Corresponding author: Deqiang Qiu.)

S. Huang, J. W. Allen and D. Qiu are with the Department of Radiology and Imaging Sciences, J. J. Lah is with the Department of Neurology, Emory University, Atlanta, GA 30322 (e-mail: shuai.huang@emory.edu; jlah@emory.edu; jason.w.allen@emory.edu; deqiang.qiu@emory.edu).

- 2) Reconstruction of the spin density  $\mathbf{X}_0$  and the relaxation rate  $\mathbf{R}_2^* = \frac{1}{T_2^*}$ .

They can be solved either separately via the standard approach or jointly via the alternating direction method of multipliers (ADMM) with convergence guarantee [29], [30]. The images  $\mathbf{X}_0, \mathbf{X}_i, \mathbf{R}_2^*$  can be considered to be approximately sparse in some proper basis like the wavelet basis [31]. This sparse prior information can be leveraged to improve reconstruction performance by adding regularization to promote sparse solutions. Compared to previous CS-based methods that can only apply regularization on  $\mathbf{X}_0$  and  $\mathbf{R}_2^*$ , our ADMM formulation allows us to make use of the sparse priors on multi-echo images  $\mathbf{X}_i$  and apply regularization on them as well. Experimental results show that the proposed joint recovery approach generally outperforms the state-of-the-art model-based approach, especially in the low-sampling rate regime.

We undersampled the k-space data using the Poisson disk sampling scheme [32], [33], which imposes a minimum distance  $d_{\min}$  between any two sampling locations. Note that the regular random sampling scheme is a special case of the Poisson disk sampling scheme when  $d_{\min}$  is set to 0. With a proper  $d_{\min}$ , Poisson disk sampling could achieve a much more uniform sampling distribution than the regular random sampling. In an effort to acquire incoherent measurements, we also investigated the use of sampling patterns that are complementary at different echo times to increase the overall coverage of k-space across multiple echoes. We conducted experiments to study how this could affect the performance in  $T_2^*$  mapping, and find that using complementary sampling patterns performs slightly better than using identical sampling pattern across different echoes. In practice we can keep the sampling pattern fixed across different echo times to simplify the pulse sequence programming on the MRI scanner.

#### A. Prior Work

Parallel imaging coupled with multi-channel phase-array coils is a widely adopted method that explores the redundancy in receiver coils to allow undersampling in the k-space [34]–[36]. It is a generic method in that it is not designed for a specific clinical task, but can be used in various MRI applications. In this paper we use multi-channel phase-array coils to improve the signal-to-noise ratio (SNR) of the reconstruction. Both the  $T_2^*$  and  $T_2$  relaxations can be modeled by a monoexponential decay of the transverse magnetization. As a result, the methods developed for  $T_2^*$  and  $T_2$  mappings can be used interchangeably. In the following we shall review previous works on reconstructing  $T_2^*$  and  $T_2$  mappings from undersampled data together.

Various approaches have been proposed to perform  $T_2$  mapping. For example, echo sharing is used to reconstruct  $T_2$ -weighted images from a single radial fast spin echo (SE) dataset [37], [38]. The multi-echo images are first reconstructed by mixing different data acquired at specific echo times in the central k-space region with the same radial data in the outer k-space region. The  $T_2$  map can then be obtained via pixel-wise monoexponential fits of the  $T_2$ -weighted images. However, the mixing of high frequency TE data introduces

errors to the high frequency details in the  $T_2$  map. To avoid mixing different echo data, model-based iterative approaches can be used to directly reconstruct the spin density  $\mathbf{X}_0$  and the relaxation rate  $\mathbf{R}_2$  from the radial fast SE data [39], [40]. A nonlinear inverse approach that minimizes the regularized least squared error using conjugate gradient (CG) was proposed in [39]. Due to the nonlinearity of the exponential decay, the CG method is sensitive to the scaling of  $\mathbf{R}_2$ . Its speed and success heavily depend on choosing a suitable scaling factor. A data-driven method can be used to estimate the scaling factor based on low resolution reconstructions from central k-space data [40]. Alternatively, the nonlinear exponential decay can be approximated by a linear combination of several pre-computed principal components, thus eliminating the need for scaling [41].

As shown in (1),  $T_2^*$  is shorter than  $T_2$  due to magnetic field inhomogeneity. The SNRs of the measurements thus decrease faster, creating a signal floor offset at longer echo times in the GRE sequence. The monoexponential decay model no longer accurately describes the signal decay across multiple echoes. A constant  $C$  was added to the monoexponential model  $\mathbf{X}_i = \mathbf{X}_0 \cdot \exp(-t_i \cdot \mathbf{R}_2^*) + C$  in [42] to correct the signal floor offset. Another method is to truncate the measurements that do not fit into the monoexponential model at longer echo times [43], [44]. Both methods have their pros and cons in estimating  $\mathbf{R}_2^*$ . Empirically, the offset method tends to produce higher  $R2^*$  values than the truncation method [45]. In this paper we use the truncation methods when performing  $T_2^*$  mapping.

#### B. Our Contribution and Paper Outline

We propose to formulate the reconstruction of  $T_2^*$  mapping from undersampled data into two subproblems: one that recovers the  $T_2^*$ -weighted images  $\mathbf{X}_i$  at each echo time, and one that recovers the spin density  $\mathbf{X}_0$  and the relaxation rate  $\mathbf{R}_2^*$ . The two subproblems can be solved either separately via the standard approach or jointly via the ADMM approach with convergence guarantee. Compared to previous approaches that only enforce sparse priors on  $\mathbf{X}_0$  and  $\mathbf{R}_2^*$ , our formulation allows us to make use of additional sparse priors on  $\mathbf{X}_i$  to obtain better reconstructions. To avoid the exhaustive search for a proper scaling factor of  $\mathbf{R}_2^*$  due to the nonlinearity of the monoexponential decay model, we derive an approximated linear model to compute the regularized least square fit of  $\mathbf{X}_0$  and  $\mathbf{R}_2^*$ . Experimental results show that the proposed approach outperforms the state-of-the-art model-based approach, especially in the low-sampling rate regime.

This paper proceeds as follows. In Section II we present the problem formulation of the  $T_2^*$  mapping, and introduce the proposed decoupled and joint recovery approaches. In Section III we solve the joint recovery problem using ADMM, show that the simpler decoupled problem is equivalent to one ADMM iteration of the joint recovery problem, and perform the convergence analysis. In Section IV we compare the proposed approaches with the state-of-the-art model-based approach by performing image reconstruction experiments from *in vivo* data under varying sampling rates. We also compare the effects of different k-space undersampling schemes. We finally conclude this paper with a discussion in Section V.

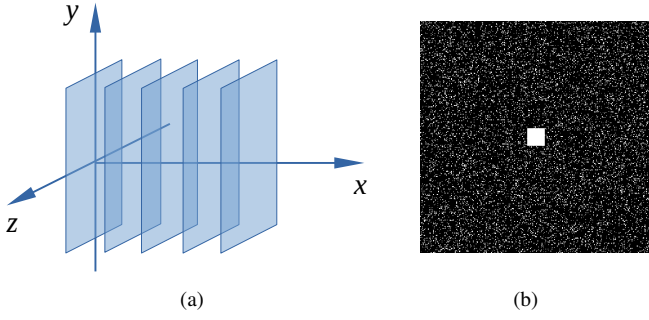


Fig. 1. (a) Undersampling in the k-space takes place in the plane determined by the two phase encoding directions  $y$  and  $z$ , whereas the readout direction  $x$  is fully sampled; (b) The Poisson disk sampling pattern in the  $y$ - $z$  plane, the central k-space is fully sampled and used to estimate the sensitivity maps of the receiver coils.

## II. PROBLEM FORMULATION

In this paper we aim to develop a fast 3D imaging method that allows us to reconstruct  $T_2^*$  maps along with spin (proton) density maps and phase images from undersampled k-space data. As shown in Fig. 1, undersampling takes place in the plane of the two phase encoding directions  $y$  and  $z$ , whereas the readout direction  $x$  is fully sampled. The Poisson disk sampling scheme is used to select the sampling locations in the  $y$ - $z$  plane, it imposes a minimum pairwise distance constraint between any two sampling locations, producing a more uniform sampling distribution than random sampling. By performing 1D FFT on the 3D k-space data along the readout direction, we can get 2D k-space data from different 2D slices. This further enables us to reconstruct the maps from multiple slices in parallel to save time. We thus focus on 2D reconstructions in the following discussion, which can be easily extended to the 3D case in a straightforward manner.

As shown in Fig. 2, the k-space data is sampled at multiple echo times (TE) within one repetition time (TR) of a gradient-echo sequence (GRE). The magnetization at every voxel across different echo times can be modeled by the exponential decay [9]

$$\mathbf{X}_i = \mathbf{X}_0 \cdot \exp(-t_i \cdot \mathbf{R}_2^*), \quad (2)$$

where  $\mathbf{X}_i$  is the  $i$ -th echo image at the time  $t_i$ ,  $\mathbf{X}_0$  is the spin density image, and  $\mathbf{R}_2^* = \frac{1}{T_2^*}$  is the relaxation rate image. Multiple receiver coils are used to acquire the measurements to improve the overall SNR. Let  $\mathbf{Y}_{ij}$  denote the measurements from the  $j$ -th receiver coil at time  $t_i$ . We have

$$\mathbf{Y}_{ij} = \mathbf{A}_i \mathbf{S}_j \mathbf{Z}_i \mathbf{X}_0 \cdot \exp(-t_i \cdot \mathbf{R}_2^*), \quad (3)$$

where  $\mathbf{A}_i = \mathbf{P}_i \mathbf{F}$  is the sampling operator at the time  $t_i$ , with  $\mathbf{P}_i$  and  $\mathbf{F}$  being the undersampling matrix and Fourier operator respectively,  $\mathbf{S}_j$  is the sensitivity map of the  $j$ -th receiver coil,  $\mathbf{Z}_i$  is the phase image at the time  $t_i$ .  $\mathbf{S}_j$ ,  $\mathbf{Z}_i$ ,  $\mathbf{X}_0$ ,  $\mathbf{R}_2^*$  are all functions of locations and are represented as discrete images. The sensitivity map  $\mathbf{S}_j$  can be estimated using the ESPIRiT approach [46]. Here we would like to recover  $\mathbf{R}_2^*$  along with  $\mathbf{X}_0$ ,  $\mathbf{Z}_i$  from the undersampled measurements  $\mathbf{Y}_{ij}$ .

### A. $T_2^*$ Mapping via Multi-echo Regularization

Since both the  $T_2$  and  $T_2^*$  relaxations of the transverse magnetization can be described in (2), the methods developed for

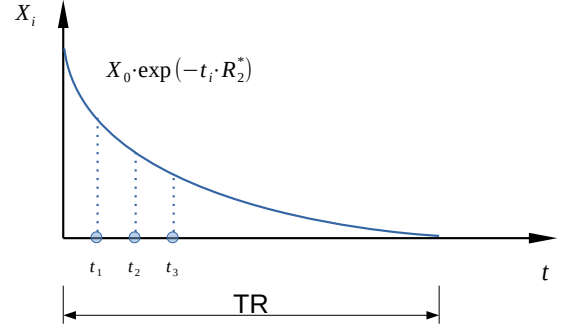


Fig. 2. The signal magnitude follows the monoexponential decay model. For the  $T_2^*$  mapping, the k-space data is sampled at multiple echo times (TE)  $t_i$  within one repetition time (TR) of a gradient-echo (GRE) sequence.

$T_2$  and  $T_2^*$  mappings can be used interchangeably. Conjugate gradient has been used to perform the least square fit of the monoexponential decay model [39]. However, due to the nonlinearity of the model, proper scaling between  $\mathbf{X}_0$  and  $\mathbf{R}_2^*$  is needed to achieve convergence within a reasonable time, and the choice of the scaling parameter is data-dependent and sensitive [40]. By taking the “log” of both sides of (2), we can establish a linear relationship between  $\log \mathbf{X}_0$  and  $\mathbf{R}_2^*$

$$\log \mathbf{X}_i = \log \mathbf{X}_0 - t_i \cdot \mathbf{R}_2^*. \quad (4)$$

Although the least square fit of the above (4) can be obtained easily, it puts higher weights on the measurements acquired at later (larger) echo times that have lower SNR [47]. In this paper we shall perform a *weighted* least square fit of (4) and minimize the following loss function

$$\sum_i x_i^2 \cdot (\log x_0 - t_i \cdot r_2^* - \log x_i)^2 = \sum_i w_i \cdot e_i. \quad (5)$$

A weight  $w_i = x_i^2$  is multiplied to the least square error  $e_i$  at time  $t_i$ :

$$\begin{aligned} e_i &= (\log x_0 - t_i \cdot r_2^* - \log x_i)^2 \\ &= \log^2(p_i + 1), \end{aligned} \quad (6)$$

where  $p_i = \frac{x_0 \exp(-t_i \cdot r_2^*) - x_i}{x_i}$ . In fact, if we take the first order approximation of  $\log(p_i + 1)$  using the Mercator series when  $p_i$  is small, we can get the least square fit of the original monoexponential decay model. Specifically, we have

$$\log(p_i + 1) = p_i - \frac{p_i^2}{2} + \frac{p_i^3}{3} - \frac{p_i^4}{4} + \dots \quad (7)$$

Ignoring the terms of second order and beyond, we can get  $\log(p_i + 1) \approx p_i$  when  $p_i$  is small. Plugging it into (5), we have

$$\sum_i x_i^2 \cdot (\log x_0 - t_i \cdot r_2^* - \log x_i)^2 \approx \sum_i (x_0 \exp(-t_i \cdot r_2^*) - x_i)^2.$$

We can see that the “weighted least square fit” of the linearized model in (4) can be viewed as an *approximation* to the “least square fit” of the monoexponential decay model in (2).

The images  $\mathbf{X}_i$ ,  $\mathbf{X}_0$ ,  $\mathbf{R}_2^*$  can be considered to be approximately sparse in some proper basis such as the wavelet basis [31]. Previous methods only enforce the sparse prior information during reconstruction via the regularization on  $\mathbf{X}_0$  and  $\mathbf{R}_2^*$  [39], [41], [48]. In this paper we shall reformulate the

reconstruction problem and introduce additional regularization on the multi-echo images  $\mathbf{X}_i$ . This way we could take full advantage of the sparse priors on all the images and achieve better reconstruction performance.

There are two ways to approach the reconstruction of  $\mathbf{X}_i, \mathbf{X}_0, \mathbf{R}_2^*$ . The first way is to decouple the problem into the reconstruction of  $\mathbf{X}_i$  and the reconstruction of  $\mathbf{X}_0, \mathbf{R}_2^*$ . The second way is to reconstruct  $\mathbf{X}_i, \mathbf{X}_0, \mathbf{R}_2^*$  jointly. Letting  $\mathbf{A}_{ij} = \mathbf{A}_i \mathbf{S}_j$  and  $\mathbf{H}_0 = \log \mathbf{X}_0$ , we have the following two problems:

1) *The decoupled recovery:*

$$\min_{\mathbf{Z}_i, \mathbf{X}_i} \sum_{ij} \|\mathbf{Y}_{ij} - \mathbf{A}_{ij} \mathbf{Z}_i \mathbf{X}_i\|_2^2 + \lambda_1 \sum_i \|\Phi(\mathbf{X}_i)\|_1 \quad (8)$$

$$\min_{\mathbf{H}_0, \mathbf{R}_2^*} \sum_i \mathbf{X}_i^2 \|\mathbf{H}_0 - t_i \mathbf{R}_2^* - \log \mathbf{X}_i\|_2^2 + \lambda_2 \|\Phi(\mathbf{H}_0)\|_1 + \lambda_3 \|\Phi(\mathbf{R}_2^*)\|_1, \quad (9)$$

where  $\sum_{ij} \|\mathbf{Y}_{ij} - \mathbf{A}_{ij} \mathbf{Z}_i \mathbf{X}_i\|_2^2$  is the data fidelity term,  $\Phi(\cdot)$  is the wavelet transform,  $\{\lambda_1, \lambda_2, \lambda_3\}$  are the regularization parameters,  $\{\lambda_1 \|\Phi(\mathbf{X}_i)\|_1, \lambda_2 \|\Phi(\mathbf{H}_0)\|_1, \lambda_3 \|\Phi(\mathbf{R}_2^*)\|_1\}$  are the regularization terms to enforce the sparse priors on  $\{\mathbf{X}_i, \mathbf{H}_0, \mathbf{R}_2^*\}$ , and  $\sum_i \mathbf{X}_i^2 \|\mathbf{H}_0 - t_i \mathbf{R}_2^* - \log \mathbf{X}_i\|_2^2$  is the *weighted* least square loss to enforce the monoexponential decay model in (2). In this paper, we use the sparsity averaging method [49] to construct an over-complete wavelet basis  $\Phi(\cdot)$  by concatenating Db1-Db8 wavelets [31].

2) *The joint recovery:*

$$\min_{\mathbf{Z}_i, \mathbf{X}_i, \mathbf{H}_0, \mathbf{R}_2^*} \sum_{ij} \|\mathbf{Y}_{ij} - \mathbf{A}_{ij} \mathbf{Z}_i \mathbf{X}_i\|_2^2 + \lambda_1 \sum_i \|\Phi(\mathbf{X}_i)\|_1 + \lambda \sum_i \mathbf{X}_i^2 \|\mathbf{H}_0 - t_i \mathbf{R}_2^* - \log \mathbf{X}_i\|_2^2 + \lambda \cdot \lambda_2 \|\Phi(\mathbf{H}_0)\|_1 + \lambda \cdot \lambda_3 \|\Phi(\mathbf{R}_2^*)\|_1, \quad (10)$$

where  $\lambda$  is the regularization parameter that balances the trade-off between the measurement model in (3) and monoexponential decay model in (2).

Later in section III we propose to solve the joint recovery using ADMM. The decoupled recovery can then be viewed as one ADMM iteration in the joint recovery. Although the decoupled recovery is obviously easier to solve, the joint recovery is more robust when there are insufficient measurements. In fact, when the sampling rate is high, the two approaches perform almost equally well. When the sampling rate is low, the joint recovery performs much better than the decoupled recovery.

### III. PROPOSED APPROACH

Since the decoupled recovery simply amounts to one ADMM iteration in the joint recovery under the right choice of parameters, we shall focus on solving the joint recovery problem using ADMM in this section. For the joint recovery of  $\{\mathbf{Z}_i, \mathbf{X}_i, \mathbf{H}_0, \mathbf{R}_2^*\}$ , the nonconvex problem in (10) is difficult to solve directly. We can use ADMM [29] to decompose it into two easier subproblems, corresponding to the optimization of  $\mathbf{Z}_i, \mathbf{X}_i$  and the optimization of  $\mathbf{H}_0, \mathbf{R}_2^*$  respectively. To make

it clearer, the objective function can be separated into two parts:

$$\min_{\mathbf{Z}_i, \mathbf{X}_i, \mathbf{H}_0, \mathbf{R}_2^*} f(\mathbf{Z}_i, \mathbf{X}_i) + \lambda \cdot g(\mathbf{X}_i, \mathbf{H}_0, \mathbf{R}_2^*), \quad (11)$$

where

$$f(\mathbf{Z}_i, \mathbf{X}_i) = \sum_{ij} \|\mathbf{Y}_{ij} - \mathbf{A}_{ij} \mathbf{Z}_i \mathbf{X}_i\|_2^2 + \lambda_1 \sum_i \|\Phi(\mathbf{X}_i)\|_1 \quad (12)$$

$$g(\mathbf{X}_i, \mathbf{H}_0, \mathbf{R}_2^*) = \sum_i \mathbf{X}_i^2 \|\mathbf{H}_0 - t_i \mathbf{R}_2^* - \log \mathbf{X}_i\|_2^2 + \lambda_2 \|\Phi(\mathbf{H}_0)\|_1 + \lambda_3 \|\Phi(\mathbf{R}_2^*)\|_1. \quad (13)$$

This is equivalent to the following constrained problem

$$\min_{\mathbf{Z}_i, \mathbf{X}_i, \mathbf{H}_0, \mathbf{R}_2^*, \mathbf{E}_i} f(\mathbf{Z}_i, \mathbf{X}_i) + \lambda \cdot g(\mathbf{E}_i, \mathbf{H}_0, \mathbf{R}_2^*) \quad (14)$$

subject to  $\mathbf{X}_i = \mathbf{E}_i$ .

Although ADMM was originally proposed to solve convex problems, it has been used with success in various nonconvex problems as well. Following the sufficient conditions introduced in [30], the convergence analysis of the proposed ADMM approach to solve (14) is discussed later in section III-D. Specifically, the augmented Lagrangian of the ADMM formulation to perform  $T_2^*$  mapping is

$$\mathcal{L}_\rho = f(\mathbf{Z}_i, \mathbf{X}_i) + \lambda \cdot g(\mathbf{E}_i, \mathbf{H}_0, \mathbf{R}_2^*) + \sum_i \mathbf{B}_i (\mathbf{X}_i - \mathbf{E}_i) + \frac{\rho}{2} \|\mathbf{X}_i - \mathbf{E}_i\|_2^2, \quad (15)$$

where  $\mathbf{B}_i$  contains the dual variables, and  $\rho$  is the regularization parameter that enforces the equality constraint  $\mathbf{X}_i = \mathbf{E}_i$ . The ADMM updates of the solutions are

1) Solve for  $\mathbf{Z}_i, \mathbf{X}_i$ :

$$\min_{\mathbf{Z}_i, \mathbf{X}_i} \sum_{ij} \|\mathbf{Y}_{ij} - \mathbf{A}_{ij} \mathbf{Z}_i \mathbf{X}_i\|_2^2 + \lambda_1 \sum_i \|\Phi(\mathbf{X}_i)\|_1 + \sum_i \mathbf{B}_i (\mathbf{X}_i - \mathbf{E}_i) + \frac{\rho}{2} \|\mathbf{X}_i - \mathbf{E}_i\|_2^2. \quad (16)$$

2) Solve for  $\mathbf{H}_0, \mathbf{R}_2^*$ :

$$\min_{\mathbf{H}_0, \mathbf{R}_2^*} \sum_i \mathbf{E}_i^2 \|\mathbf{H}_0 - t_i \mathbf{R}_2^* - \log \mathbf{E}_i\|_2^2 + \lambda_2 \|\Phi(\mathbf{H}_0)\|_1 + \lambda_3 \|\Phi(\mathbf{R}_2^*)\|_1. \quad (17)$$

3) Solve for  $\mathbf{E}_i$ :

$$\min_{\mathbf{E}_i} \mathbf{E}_i^2 \|\mathbf{H}_0 - t_i \mathbf{R}_2^* - \log \mathbf{E}_i\|_2^2 + \mathbf{B}_i (\mathbf{X}_i - \mathbf{E}_i) + \frac{\rho}{2} \|\mathbf{X}_i - \mathbf{E}_i\|_2^2. \quad (18)$$

4) Update  $\mathbf{B}_i$ :

$$\mathbf{B}_i = \mathbf{B}_i + \rho (\mathbf{X}_i - \mathbf{E}_i). \quad (19)$$

We can see that when  $\mathbf{B}_i = \mathbf{0}$ ,  $\rho = 0$  and  $\mathbf{X}_i = \mathbf{E}_i$ , the subproblems (16), (17) then become the decoupled recovery in (8), (9). The subproblems in (16)-(18) are easier to solve compared to the original joint recovery problem in (10). We next show how they can be solved one by one.

### A. Computation of $Z_i$ and $X_i$

We proceed to solve (16) using the proximal gradient method iteratively until convergence [50], [51]. Let  $\mathbf{U}_i = \mathbf{Z}_i \mathbf{X}_i$  and  $f_j(\mathbf{U}_i) = \|\mathbf{Y}_{ij} - \mathbf{A}_{ij} \mathbf{U}_i\|_2^2$ . In the  $(k+1)$ -th iteration, we perform the proximal regularization on it with respect to the solution  $\mathbf{U}_i^{(k)}$  from the previous  $k$ -th iteration.

$$\begin{aligned} f_j(\mathbf{U}_i) &\leq f_j(\mathbf{U}_i^{(k)}) + \langle \mathbf{U}_i - \mathbf{U}_i^{(k)}, \nabla f_j(\mathbf{U}_i^{(k)}) \rangle \\ &\quad + \langle \bar{\mathbf{U}}_i - \bar{\mathbf{U}}_i^{(k)}, \nabla f_j(\bar{\mathbf{U}}_i^{(k)}) \rangle + \frac{\kappa_{ij}}{2} \|\mathbf{U}_i - \mathbf{U}_i^{(k)}\|_2^2 \\ &= \frac{\kappa_{ij}}{2} \|\mathbf{U}_i - \mathbf{U}_i^{(k)}\|_2^2 + \mathcal{O}(\mathbf{U}_i^{(k)}), \end{aligned}$$

where  $\kappa_{ij}$  is the Lipschitz constant of  $f_j(\mathbf{U}_i)$  to ensure the above proximal regularization holds,  $\bar{\mathbf{U}}_i$  is the conjugate of  $\mathbf{U}_i$ ,  $\mathcal{O}(\mathbf{U}_i^{(k)})$  is some constant that depends on the previous solution  $\mathbf{U}_i^{(k)}$ , the gradient  $\nabla f_j(\mathbf{U}_i)$  and  $\mathbf{Q}_{ij}^{(k)}$  are as follows

$$\nabla f_j(\mathbf{U}_i) = \left( \frac{\partial f_j(\mathbf{U}_i)}{\partial \mathbf{U}_i} \right)^* = \mathbf{A}_{ij}^* \mathbf{A}_{ij} \mathbf{U}_i - \mathbf{A}_{ij}^* \mathbf{Y}_{ij} \quad (20)$$

$$\mathbf{Q}_{ij}^{(k)} = \mathbf{U}_i^{(k)} - \frac{2}{\kappa_{ij}} \nabla f_j(\mathbf{U}_i^{(k)}). \quad (21)$$

Following the FISTA approach [50], we then solve the following problem in the  $(k+1)$ -th iteration

$$\begin{aligned} \min_{\mathbf{Z}_i, \mathbf{X}_i} \quad &\sum_j \frac{\kappa_{ij}}{2} \|\mathbf{Z}_i \mathbf{X}_i - \mathbf{Q}_{ij}^{(k)}\|_2^2 + \lambda_1 \sum_i \|\Phi(\mathbf{X}_i)\|_1 \\ &+ \sum_i \mathbf{B}_i(\mathbf{X}_i - \mathbf{E}_i) + \frac{\rho}{2} \|\mathbf{X}_i - \mathbf{E}_i\|_2^2. \end{aligned} \quad (22)$$

1) *Computation of  $Z_i$* : Let  $\mathbf{Z}_i = \exp(j\boldsymbol{\Theta}_i)$ , where  $\boldsymbol{\Theta}_i \in [0, 2\pi)$  is the angle of the phase image. We then have

$$\min_{\boldsymbol{\Theta}_i} \sum_j \frac{\kappa_{ij}}{2} \|\mathbf{X}_i \exp(j\boldsymbol{\Theta}_i) - \mathbf{Q}_{ij}^{(k)}\|_2^2. \quad (23)$$

Setting the first order derivative of (23) to zero, we have

$$\frac{\sin \boldsymbol{\Theta}_i}{\cos \boldsymbol{\Theta}_i} = \frac{\sum_j \kappa_{ij} \text{Im}(\mathbf{Q}_{ij}^{(k)})}{\sum_j \kappa_{ij} \text{Re}(\mathbf{Q}_{ij}^{(k)})}. \quad (24)$$

There are two solutions that satisfy (24). In order to find the minimizing solution, we further compute the second order derivative of (23)

$$\frac{\partial^2}{\partial \boldsymbol{\Theta}_i^2} = \mathbf{X}_i \left( \cos \boldsymbol{\Theta}_i \sum_j \kappa_{ij} \text{Re}(\mathbf{Q}_{ij}^{(k)}) + \sin \boldsymbol{\Theta}_i \sum_j \kappa_{ij} \text{Im}(\mathbf{Q}_{ij}^{(k)}) \right). \quad (25)$$

The above (25) is positive if  $\cos \boldsymbol{\Theta}_i$  has the same sign as  $\sum_j \kappa_{ij} \text{Re}(\mathbf{Q}_{ij}^{(k)})$  and  $\sin \boldsymbol{\Theta}_i$  has the same sign as  $\sum_j \text{Im}(\mathbf{Q}_{ij}^{(k)})$ . Hence the minimizing  $\boldsymbol{\Theta}_i$  is

$$\boldsymbol{\Theta}_i = \text{Ang} \left( \sum_j \kappa_{ij} \text{Re}(\mathbf{Q}_{ij}^{(k)}) + j \sum_j \kappa_{ij} \text{Im}(\mathbf{Q}_{ij}^{(k)}) \right), \quad (26)$$

where  $\text{Ang}(\cdot)$  computes the angle of a complex number.

2) *Computation of  $X_i$* : We further apply the proximal regularization on  $f_j(\mathbf{X}_i) = \|\mathbf{Z}_i \mathbf{X}_i - \mathbf{Q}_{ij}^{(k)}\|_2^2$  in (22).

$$f_j(\mathbf{X}_i) \leq \frac{\alpha_i}{2} \|\mathbf{X}_i - \mathbf{P}_{ij}^{(k)}\|_2^2 + \mathcal{O}(\mathbf{X}_i^{(k)}), \quad (27)$$

where  $\alpha_i$  is the Lipschitz constant of  $f_j(\mathbf{X}_i)$  to ensure the proximal regularization holds,  $\mathcal{O}(\mathbf{X}_i^{(k)})$  is some constant that depends on the previous solution  $\mathbf{X}_i^{(k)}$ , and  $\mathbf{P}_{ij}^{(k)}$  is

$$\mathbf{P}_{ij}^{(k)} = \mathbf{X}_i^{(k)} - \frac{1}{\alpha_i} \nabla_j f_j(\mathbf{X}_i^{(k)}) = \text{Re}(\bar{\mathbf{Z}}_i \mathbf{Q}_{ij}^{(k)}). \quad (28)$$

We then solve the following  $l_1$ -minimization problem

$$\min_{\mathbf{X}_i} \sum_i \frac{1}{2} \|\mathbf{X}_i - \mathbf{V}_i^{(k)}\|_2^2 + \frac{\lambda_1}{\rho + \sum_j \kappa_{ij}} \|\Phi(\mathbf{X}_i)\|_1, \quad (29)$$

where  $\mathbf{V}_i^{(k)}$  is

$$\mathbf{V}_i^{(k)} = \frac{\sum_j \kappa_{ij} \mathbf{Q}_{ij}^{(k)} - \mathbf{B}_i + \rho \mathbf{E}_i}{\rho + \sum_j \kappa_{ij}}. \quad (30)$$

It can be easily solved using FISTA [50].

### B. Computation of $H_0$ and $R_2^*$

We use proximal gradient regularization on the following  $i(\mathbf{H}_0, \mathbf{R}_2^*)$  with respect to  $\mathbf{H}_0$  and  $\mathbf{R}_2^*$  to solve (17).

$$i(\mathbf{H}_0, \mathbf{R}_2^*) = \|\mathbf{E}_i \mathbf{H}_0 - t_i \mathbf{E}_i \mathbf{R}_2^* - \mathbf{E}_i \log \mathbf{E}_i\|_2^2 \quad (31)$$

1) *Computation of  $H_0$* : In the  $(k+1)$ -th iteration, we have

$$i(\mathbf{H}_0) \leq \frac{\gamma_i}{2} \|\mathbf{H}_0 - \mathbf{F}_i^{(k)}\|_2^2 + \mathcal{O}(\mathbf{H}_0^{(k)}), \quad (32)$$

where  $\gamma_i$  is the Lipschitz constant of  $i(\mathbf{H}_0)$  to ensure the proximal regularization holds,  $\mathcal{O}(\mathbf{H}_0^{(k)})$  is some constant that depends on the previous solution  $\mathbf{H}_0^{(k)}$ , and  $\mathbf{F}_i^{(k)}$  is

$$\mathbf{F}_i^{(k)} = \mathbf{H}_0^{(k)} - \frac{1}{\gamma_i} \nabla_i(\mathbf{H}_0^{(k)}). \quad (33)$$

We then solve the following  $l_1$ -minimization problem

$$\min_{\mathbf{H}_0} \frac{1}{2} \left\| \mathbf{H}_0 - \frac{\sum_i \gamma_i \mathbf{F}_i^{(k)}}{\sum_i \gamma_i} \right\|_2^2 + \frac{\lambda_2}{\sum_i \gamma_i} \|\Phi(\mathbf{H}_0)\|_1. \quad (34)$$

2) *Computation of  $R_2^*$* : The relaxation rate  $\mathbf{R}_2^*$  can be computed similarly. In the  $(k+1)$ -th iteration, we have

$$i(\mathbf{R}_2^*) \leq \frac{\nu_i}{2} \|\mathbf{R}_2^* - \mathbf{G}_i^{(k)}\|_2^2 + \mathcal{O}(\mathbf{R}_2^{*(k)}), \quad (35)$$

where  $\nu_i$  is the Lipschitz constant of  $i(\mathbf{R}_2^*)$  to ensure the proximal regularization holds,  $\mathcal{O}(\mathbf{R}_2^{*(k)})$  is some constant that depends on the previous solution  $\mathbf{R}_2^{*(k)}$ , and  $\mathbf{G}_i^{(k)}$  is

$$\mathbf{G}_i^{(k)} = \mathbf{R}_2^{*(k)} - \frac{1}{\nu_i} \nabla_i(\mathbf{R}_2^{*(k)}). \quad (36)$$

We then solve the following  $l_1$ -minimization problem

$$\min_{\mathbf{R}_2^*} \frac{1}{2} \left\| \mathbf{R}_2^* - \frac{\sum_i \nu_i \mathbf{G}_i^{(k)}}{\sum_i \nu_i} \right\|_2^2 + \frac{\lambda_3}{\sum_i \nu_i} \|\Phi(\mathbf{R}_2^*)\|_1. \quad (37)$$

### C. Computation of $E_i$

Let  $D_i = \log E_i$  and  $W_i = H_0 - t_i R_2^*$ . Here we assume  $E_i \in [e_{\min}, e_{\max}]$  and  $e_{\min} > 0$  is close to zero so that  $D_i$  is bounded. In practice we can choose  $e_{\min}$  to be the machine precision. The optimization problem in (18) is equivalent to

$$\begin{aligned} \min_{D_i} \quad & (D_i) = \frac{\rho}{2} \|X_i - \exp(D_i)\|_2^2 + \lambda \exp(2D_i) \|D_i - W_i\|_2^2 \\ & + B_i(X_i - \exp(D_i)), \end{aligned} \quad (38)$$

where  $D_i \in [d_{\min}, d_{\max}]$  is bounded. Although the above (19) is nonconvex, it consists of simple one-dimensional (pixel-wise) nonconvex problems. The *global* minimizing solutions occur at either the boundaries or the stationary points that make the first order derivative  $'(d_i) = 0$ .

Since  $D_i$  is bounded, we next show how to find the stationary points using the bisection method. We have

$$'(d_i) = \exp(d_i) \cdot {}_1(d_i) \quad (39)$$

$$\begin{aligned} {}_1(d_i) = & \rho(\exp(d_i) - x_i) + 2\lambda \exp(d_i) \cdot (d_i - w_i) \\ & + 2\lambda \exp(d_i) \cdot (d_i - w_i)^2 - y_i. \end{aligned} \quad (40)$$

In order to use the bisection method to find the other stationary points that make  ${}_1(d_i) = 0$ , we need to find intervals where  ${}_1(d_i)$  is monotonically increasing or decreasing. We further compute the first order derivative of  ${}_1(d_i)$  as follows

$$'{}_1(d_i) = \exp(d_i) \cdot {}_2(d_i) \quad (41)$$

$$\begin{aligned} {}_2(d_i) = & 2\lambda \cdot d_i^2 + (6\lambda - 4\lambda w_i) \cdot d_i \\ & + \rho - 6\lambda w_i + 2\lambda + 2\lambda w_i^2. \end{aligned} \quad (42)$$

The above  ${}_2(d_i)$  is a second-degree polynomial. We can find the monotonic intervals of  ${}_1(d_i)$  based on the roots of  ${}_2(d_i)$ :

- 1) If  ${}_2(d_i)$  has less than two real roots,  $'{}_1(d_i) \geq 0$ . We have that  $[d_{\min}, d_{\max}]$  is a monotonic interval of  ${}_1(d_i)$ .
- 2) If  ${}_2(d_i)$  has two real roots  $d_i(1) < d_i(2)$ . We have that
  - ${}_1(d_i)$  is increasing in  $(-\infty, d_i(1)) \cap [d_{\min}, d_{\max}]$ .
  - ${}_1(d_i)$  is decreasing in  $(d_i(1), d_i(2)) \cap [d_{\min}, d_{\max}]$ .
  - ${}_1(d_i)$  is increasing in  $(-d_i(2), \infty) \cap [d_{\min}, d_{\max}]$ .

Computing the stationary points is just the first step in finding the global minimum in (38). They could be local minimum, local maximum or a saddle point. In order to find the global minimum, we still need to compare the function values of  $q(d_i)$  at the stationary points with those at the boundaries of the monotonic intervals. Eventually, by comparing the function values of all the minimizing solutions from every monotonic interval, we can find the global minimum in (38).

### D. Convergence Analysis

ADMM has been used with success in nonconvex problems such as matrix completion [52], [53], phase retrieval [54], image denoising [55], [56], etc. Characterizing its convergence behavior under the nonconvex setting has attracted a lot of interests in recent years [30], [57], [58]. By examining the sufficient convergence conditions introduced in [30], we can analyze the behavior of ADMM for  $T_2^*$  mapping. We should note that even if the conditions are not satisfied, it does not mean that ADMM would diverge. It is still an open problem

to establish necessary and sufficient conditions for ADMM to converge under the nonconvex setting. Nonetheless, the following analysis still provides valuable insights into the factors that influence the behavior of the proposed approach.

There are two sets of variables in the constrained nonconvex problem (14):  $\mathcal{V}_1 = \{Z_i, X_i\}$  and  $\mathcal{V}_2 = \{E_i, H_0, R_2^*\}$ . In the following analysis we shall assume the feasible set  $\{\mathcal{V}_1, \mathcal{V}_2\}$  is bounded. Letting  $\Psi(\mathcal{V}_1, \mathcal{V}_2) = f(\mathcal{V}_1) + \lambda \cdot g(\mathcal{V}_2)$ , we can rewrite (14) as follows

$$\begin{aligned} \min_{\mathcal{V}_1, \mathcal{V}_2} \quad & \Psi(\mathcal{V}_1, \mathcal{V}_2) \\ \text{subject to} \quad & T_1 \mathcal{V}_1 + T_2 \mathcal{V}_2 = 0, \end{aligned} \quad (43)$$

where  $T_1, T_2$  are matrices used to create the constraint  $X_i = E_i$ . We next examine the sufficient convergence conditions outlined in [30] one by one:

- 1) The objective function  $\Psi(\mathcal{V}_1, \mathcal{V}_2)$  is coercive, that is,  $\Psi \rightarrow \infty$  when  $\|(\mathcal{V}_1, \mathcal{V}_2)\| \rightarrow \infty$ .
- 2) The images (Im) of  $T_1, T_2$  are the same,  $\text{Im}(T_1) = \text{Im}(T_2) = \text{Im}([I \ 0])$ , where  $I$  is the identity matrix and  $0$  is an all zero vector.
- 3) With  $\{Z_i, X_i\}$  fixed and  $E_i = X_i$ , we have the following problem to solve

$$\begin{aligned} \min_{H_0, R_2^*} \quad & \sum_i X_i^2 \|H_0 - t_i R_2^* - \log X_i\|_2^2 \\ & + \lambda_2 \|\Phi(H_0)\|_1 + \lambda_3 \|\Phi(R_2^*)\|_2. \end{aligned} \quad (44)$$

We need at least two echo images for (44) to have a unique solution. Since the feasible set  $\{H_0, R_2^*\}$  is bounded, the solution is Lipschitz continuous with respect to the input  $X_i$ .

- 4) With  $\{H_0, R_2^*, E_i\}$  and  $X_i$  fixed, we have the following problem to solve

$$\min_{Z_i} \quad \sum_j \|Y_{ij} - A_{ij} X_i Z_i\|_2^2, \quad (45)$$

Sufficient incoherent measurements are needed for (45) to have a unique solution. Although we are undersampling in the k-space, additional incoherent measurements can be acquired by the multiple receiver coils. Since the feasible set of  $Z_i$  is bounded, the solution is also Lipschitz continuous with respect to the input  $X_i$ .

- 5) With  $\{H_0, R_2^*, E_i\}$  and  $Z_i$  fixed, we solve the following problem subject to  $X_i = E_i$

$$\min_{X_i} \quad \sum_j \|Y_{ij} - A_{ij} Z_i X_i\|_2^2 + \lambda_1 \|\Phi(X_i)\|_1. \quad (46)$$

The above (46) simply has a unique solution  $X_i = E_i$  and the solution is Lipschitz continuous with respect to the input  $E_i$ .

In summary, apart from the assumption that the feasible set  $\{\mathcal{V}_1, \mathcal{V}_2\}$  is bounded, we need sufficient incoherent measurements by multiple receiver coils from at least two echo times so that sufficient convergence conditions would hold.

### E. Parameter Tuning

The regularization parameters  $\{\lambda_1, \lambda_2, \lambda_3, \lambda, \rho\}$  needs to be properly tuned in order to achieve best performance. With the five parameters at hand, it would be computationally inefficient

to tune them all at once. Here we take the divide-and-conquer strategy and tune them in different groups. In general, the optimal parameters  $\{\lambda_1, \lambda_2, \lambda_3\}$  obtained for the decoupled recovery in (8)-(9) can be migrated to the joint recovery. We can then fix  $\{\lambda_1, \lambda_2, \lambda_3\}$  and focus on tuning  $\{\lambda, \rho\}$  in the joint recovery. In summary, we can tune the parameters in the following order:

- 1) Find the optimal  $\lambda_1$  in (8) that recovers  $\mathbf{Z}_i, \mathbf{X}_i$ .
- 2) Find the optimal  $\lambda_2, \lambda_3$  in (9) that recover  $\mathbf{H}_0, \mathbf{R}_2^*$ .
- 3) Fix the  $\lambda_1, \lambda_2, \lambda_3$  obtained previously, find the optimal  $\lambda, \rho$  in (10) that solve the joint recovery problem.

From the *in vivo* experiments we learned that the optimal parameters are *stable* and *generalizable* on 3D MRI data that are acquired under the same protocol. This greatly simplifies the overall parameter tuning process. In practice we can tune the parameters on a fully sampled 2D slice, aka training data, and use them to reconstruct other undersampled 2D slices in a 3D volume.

#### IV. EXPERIMENTAL RESULTS

We acquired *in vivo* 3D brain data on a 3T MRI scanner (Siemens Prisma), with written consent obtained from the subject before imaging and approval from the Institutional Review Board of Emory University. The k-space was fully sampled during the acquisition to provide the ‘‘gold standard’’ references for evaluation. The undersampling took place in the phase encoding  $y - z$  plane afterwards according to the randomly generated Poisson disk sampling patterns. The readout direction  $x$  was always fully sampled at each TE. The GRE sequence was used for  $T_2^*$  mapping, and the data were acquired with a 32-channel head coil. Two acquisition protocols are adopted to acquire data from 6 subjects.

- For the first protocol, we have the number of echoes = 6, the first echo time = 7.64 ms, echo spacing = 5.41 ms, slice thickness = 0.7 mm, resolution = 0.6875 mm, pixel bandwidth = 260 Hz, TR = 40 ms, and FoV = 22 cm, which takes approximately 35 minutes to finish.
- For the second protocol, we have the number of echoes = 4, the first echo time = 7.32 ms, echo spacing = 8.68 ms, slice thickness = 0.7 mm, resolution = 0.6875 mm, pixel bandwidth = 260 Hz, TR = 38 ms, and FoV = 22 cm, which takes approximately 33 minutes to finish.

We eventually saved the fully sampled 3D k-space data in a matrix of size  $320 \times 320 \times 280$  for each subject.

As discussed in section II, the 3D reconstruction problem can be decomposed into parallelizable 2D problems to speed up the reconstruction process. In the following we shall compare different reconstruction approaches and sampling schemes on uniformly selected 2D slices that cover the region of interest. Taking the recovered  $\hat{\mathbf{R}}_2^*$  image for example, we compute the pixel-wise relative errors of the brain<sup>1</sup>  $\frac{|r_2^* - \hat{r}_2^*|}{|r_2^*|}$  according to the gold standard  $\mathbf{R}_2^*$  reconstructed from fully-sampled data, and use the average relative error of all brain pixels in the 2D slice as the comparison criterion.

<sup>1</sup>A mask is used to extract the subject’s brain.

#### A. Comparison of Reconstruction Approaches

We compare the proposed decoupled and joint recovery approaches with the state-of-the-art model-based approach that solves the following problem [39]

$$\min_{\mathbf{Z}_i, \mathbf{X}_0, \mathbf{R}_2^*} \sum_{ij} \|\mathbf{Y}_{ij} - \mathbf{A}_i \mathbf{S}_j \mathbf{Z}_i \mathbf{X}_0 \cdot \exp(-t_i \cdot \mathbf{R}_2^*)\|_2^2 + \lambda_1 \|\Phi(\mathbf{X}_0)\|_1 + \lambda_2 \|\Phi(\mathbf{R}_2^*)\|_1. \quad (47)$$

We set  $d_{\min} = 2$  in the Poisson disk sampling scheme and use different sampling patterns across the echo times. The parameters for each approach are individually tuned to achieve best performance.

We compare the three approaches on the 3D MRI dataset acquired from 6 subjects. An acquisition protocol with 6 echoes is adopted for the first three subjects, and a different acquisition protocol with 4 echoes is adopted for the other three subjects. As long as the acquisition protocol is fixed, the optimal parameters tuned on one 2D slice of a subject can be used to perform reconstruction on the other subjects. We undersample the the k-space measurements with the sampling rates varying between 10% and 50%. For each subject, we uniformly choose 20 out of 208 2D slices, and use the three approaches to recover the relaxation rate  $\mathbf{R}_2^*$  and the spin density  $\mathbf{X}_0$  from undersampled data. The average relative errors of all the 2D slices across 6 subjects are computed and shown in Fig. 3. We can see that the joint recovery approach generally performs better than the other two approaches. When the sampling rate is low ( $\sim 10\%$ ), the joint recovery approach performs much better than the decoupled approach and the model-based approach. When the sampling rate is higher ( $\geq 20\%$ ), the decoupled and joint recovery approaches perform almost equally well, with a very mild advantage from the joint recovery approach. As the sampling rate increases towards 50%, the performances of the three approaches become similar.

We next use one of the 2D slices as an example, and show the recovered  $\hat{\mathbf{R}}_2^*$  and  $\hat{\mathbf{X}}_0$  images in Fig. 4. We can see that the joint recovery approach does a much better job in reconstructing the central brain region in the low-sampling rate regime (10%). The joint recovery approach not only enforces the monoexponential decay model during the reconstruction, but also imposes the multi-echo regularization of echo images  $\mathbf{X}_i$ . This allows it to take in more prior information to help with the reconstruction from undersampled measurements. As a comparison, the decoupled approach does not incorporate the monoexponential decay model in the reconstruction of the echo images  $\mathbf{X}_i$ , while the model-based approach in (47) does not impose multi-echo regularization on the echo images  $\mathbf{X}_i$ . This puts the other two approaches in a disadvantageous position, especially when the data is highly undersampled.

#### B. Comparison of Sampling Schemes

The Poisson disk sampling scheme enforces a minimum distance  $d_{\min}$  between any two sampling locations. The choice of  $d_{\min}$  has a direct effect on the reconstruction performance, and we choose  $d_{\min} = 2$  pixels in the experiments. The undersampling process at the echo times are independent,

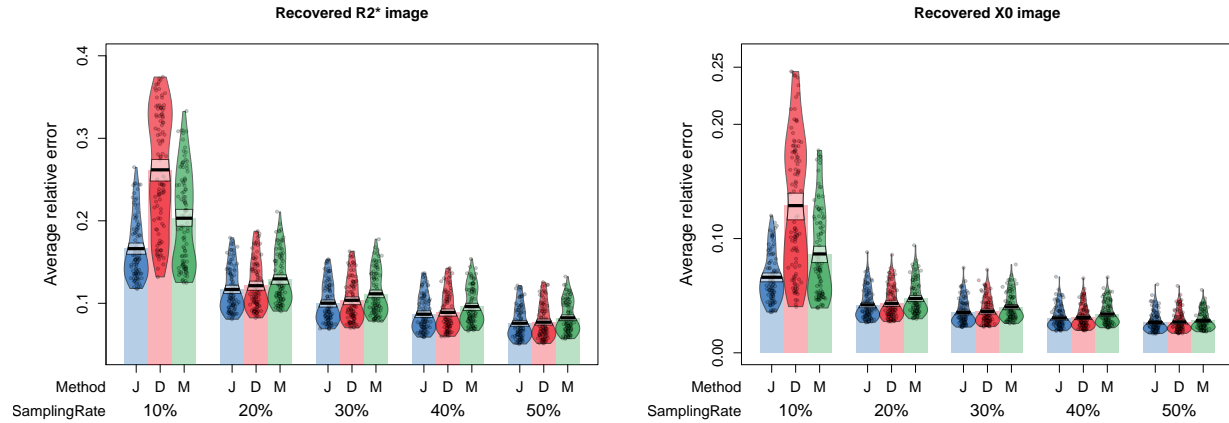


Fig. 3. Comparison of the proposed joint (J) and decoupled (D) recovery approaches with the state-of-the-art model-based (M) approach across different sampling rates. Every point here corresponds to the average relative error of all brain pixels in one 2D slice.

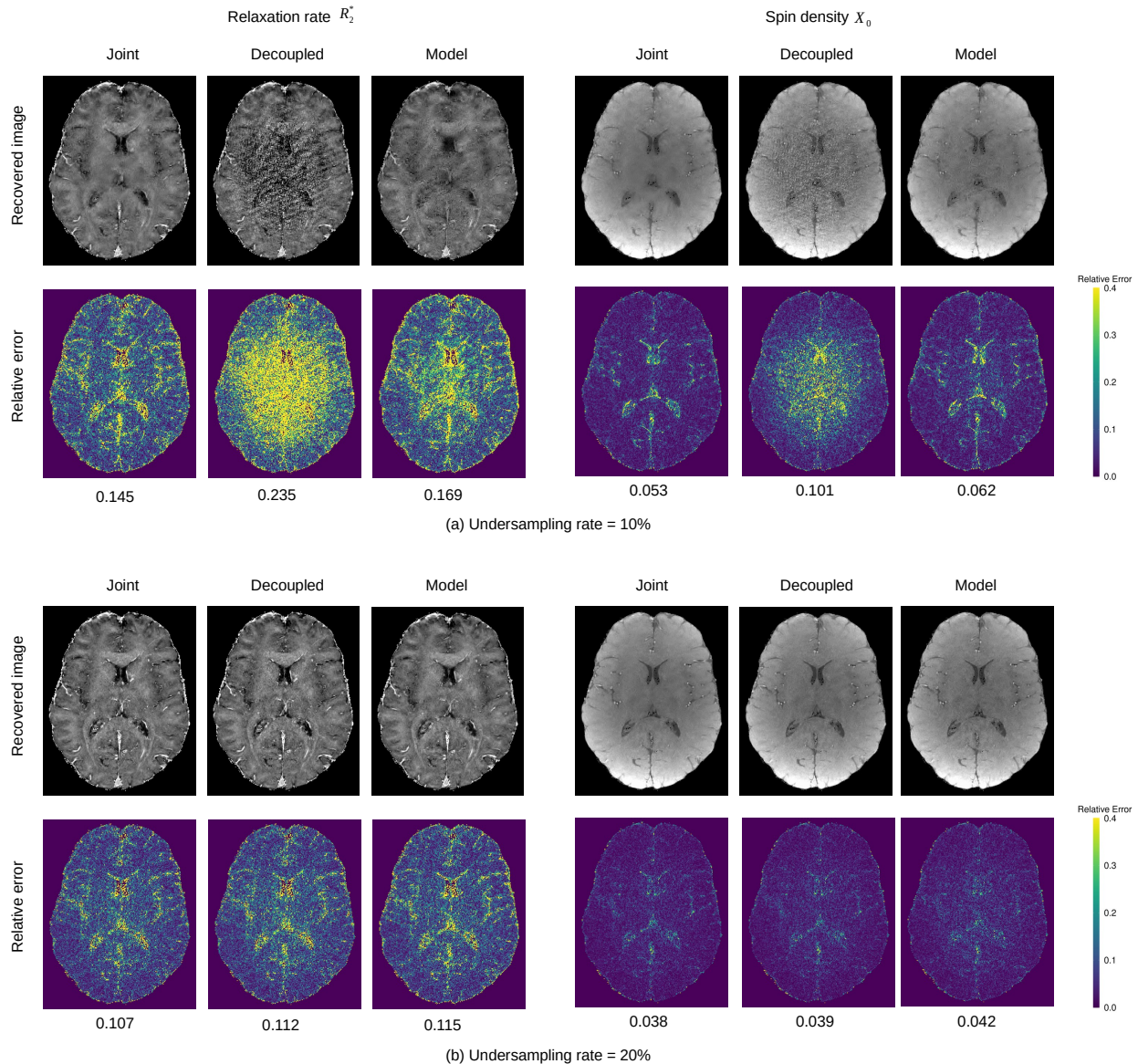


Fig. 4. The recovered  $R_2^*$  and  $X_0$  images using the proposed joint and decoupled recovery approaches, and the state-of-the-art model-based approach when the undersampling rates are 10% and 20%.

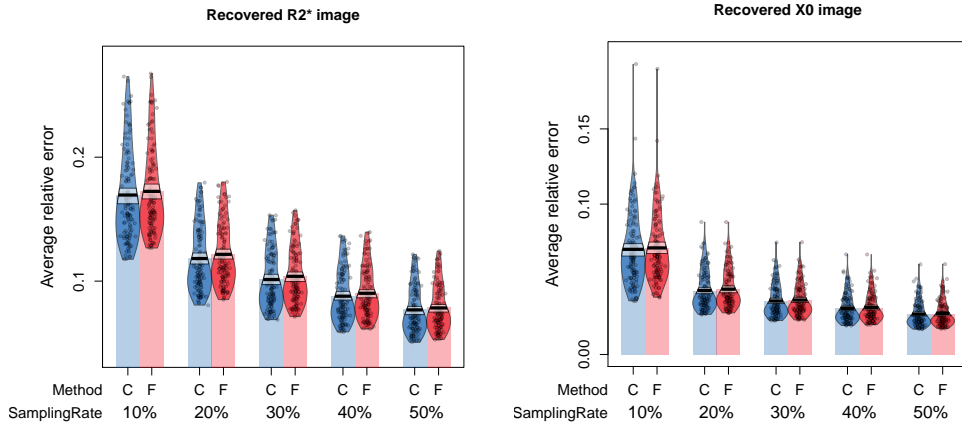


Fig. 5. Comparison of the complimentary (C) and fixed (F) Poisson disk sampling patterns in the joint recovery approach across different sampling rates. Every point here corresponds to the average relative error of all brain pixels in one 2D slice.

which gives us the freedom to choose different sampling patterns at different echo times. Using the joint recovery approach for reconstruction, we next compare the case where the sampling patterns are fixed and the case where the sampling patterns are complementary to one another across different echoes. The experimental settings are kept the same as in section IV-A. The average relative errors of the recovered  $\hat{R}_2^*$  and  $\hat{X}_0$  images are shown in Fig. 5. We can see that the two types of sampling patterns perform almost equally well. The complementary sampling patterns perform only slightly better. Based on this experiment, we can keep the sampling pattern fixed across different echoes without sacrificing the reconstruction performance too much, thus simplifying the pulse sequence programming on the MRI scanner.

## V. CONCLUSION AND DISCUSSION

In this paper we aim to develop fast 3D  $T_2^*$  imaging method that reconstructs the relaxation rate  $R_2^* = \frac{1}{T_2^*}$  and the spin density  $X_0$  from undersampled measurements in quantitative MRI. We formulate the reconstruction problem into two sub-problems: one that recovers the multi-echo images  $X_i$ , and one that recovers  $R_2^*, X_0$ . They can be solved separately via the standard approach or jointly the ADMM. Compared to previous approaches that only enforce sparse priors on  $X_0$  and  $R_2^*$ , the propose approach makes use of additional sparse priors on the multi-echo images  $X_i$  during the reconstruction. To avoid the scaling issue caused by the nonlinearity of the monoexponential decay model, we further derive its linear approximation to compute the regularized least square fit of  $X_0$  and  $R_2^*$ . Experimental results show that the proposed joint recovery approach generally outperforms the state-of-the-art model-based approach, especially in the low-sampling rate regime.

The reconstruction of  $R_2^*$  and  $X_0$  is inherently a nonconvex problem. With the linear approximation of the monoexponential decay model, the decoupled approach in (8)-(9) becomes convex and is easy to solve. However, it performs much worse than the nonconvex joint recovery approach in the low-sampling rate regime. We showed in section III-D that the ADMM used in joint recovery could still achieve convergence in the nonconvex setting when sufficient incoherent measurements are sampled from at least two echo times. When the

sampling rate is high, the decoupled and joint approaches perform almost equally well. In this case, we can simply choose the decoupled approach for reconstruction.

## REFERENCES

- [1] F. Fazekas, R. Kleinert, G. Roob, G. Kleinert, P. Kapeller, R. Schmidt, and H.-P. Hartung, "Histopathologic analysis of foci of signal loss on gradient-echo  $t_2^*$ -weighted mr images in patients with spontaneous intracerebral hemorrhage: Evidence of microangiopathy-related microbleeds," *AJNR Am J Neuroradiol*, vol. 20, no. 4, pp. 637–642, 1999.
- [2] T. Kinoshita, T. Okudera, H. Tamura, T. Ogawa, and J. Hatazawa, "Assessment of lacunar hemorrhage associated with hypertensive stroke by echo-planar gradient-echo  $t_2^*$ -weighted mri," *Stroke*, vol. 31, no. 7, pp. 1646–1650, 2000.
- [3] D. P. O'Regan, R. Ahmed, N. Karunanithy, C. Neuwirth, Y. Tan, G. Durighel, J. V. Hajnal, I. Nadra, S. J. Corbett, and S. A. Cook, "Reperfusion hemorrhage following acute myocardial infarction: Assessment with  $t_2^*$  mapping and effect on measuring the area at risk," *Radiology*, vol. 250, no. 3, pp. 916–922, 2009.
- [4] N. Yamada, S. Imakita, T. Sakuma, and M. Takamiya, "Intracranial calcification on gradient-echo phase image: depiction of diamagnetic susceptibility," *Radiology*, vol. 198, no. 1, pp. 171–178, 1996.
- [5] R. Gupta, S. Rao, R. Jain, L. Pal, R. Kumar, S. Venkatesh, and R. Rathore, "Differentiation of calcification from chronic hemorrhage with corrected gradient echo phase imaging," *Journal of Computer Assisted Tomography*, vol. 25, no. 5, pp. 698–704, Sept. 2001.
- [6] L. Anderson, S. Holden, B. Davis, E. Prescott, C. Charrier, N. Bunce, D. Firmin, B. Wonke, J. Porter, J. Walker, and D. Pennell, "Cardiovascular T2-star ( $T_2^*$ ) magnetic resonance for the early diagnosis of myocardial iron overload," *European Heart Journal*, vol. 22, no. 23, pp. 2171–2179, 12 2001.
- [7] A. McNeill, D. Birchall, S. J. Hayflick, A. Gregory, J. F. Schenk, E. A. Zimmerman, H. Shang, H. Miyajima, and P. F. Chinnery, " $T_2^*$  and fse mri distinguishes four subtypes of neurodegeneration with brain iron accumulation," *Neurology*, vol. 70, no. 18, pp. 1614–1619, 2008.
- [8] D. D. Stark and W. G. Bradley, *Magnetic Resonance Imaging*, 3rd ed, Mosby Inc., St. Louis, MO, USA, 2006.
- [9] D. G. Nishimura, *Principles of Magnetic Resonance Imaging*, Stanford University, Stanford, CA, USA, 2010.
- [10] G. B. Chavhan, P. S. Babyn, B. Thomas, M. M. Shroff, and E. M. Haacke, "Principles, techniques, and applications of  $t_2^*$ -based mr imaging and its special applications," *RadioGraphics*, vol. 29, no. 5, pp. 1433–1449, 2009.
- [11] E. Haacke, S. Mittal, Z. Wu, J. Neelavalli, and Y.-C. Cheng, "Susceptibility-weighted imaging: Technical aspects and clinical applications, part 1," *AJNR Am J Neuroradiol*, vol. 30, no. 1, pp. 19–30, 2009.
- [12] S. Mittal, Z. Wu, J. Neelavalli, and E. Haacke, "Susceptibility-weighted imaging: Technical aspects and clinical applications, part 2," *AJNR Am J Neuroradiol*, vol. 30, no. 2, pp. 232–252, 2009.
- [13] S. Cha, E. A. Knopp, G. Johnson, S. G. Wetzel, A. W. Litt, and D. Zagzag, "Intracranial mass lesions: Dynamic contrast-enhanced susceptibility-weighted echo-planar perfusion mr imaging," *Radiology*, vol. 223, no. 1, pp. 11–29, 2002.

- [14] M. A. Weber, S. Zoubaa, M. Schlieter, E. Jüttler, H. B. Huttner, K. Geletneký, C. Ittrich, M. P. Lichy, A. Kroll, J. Debus, F. L. Giesel, M. Hartmann, and M. Essig, "Diagnostic performance of spectroscopic and perfusion mri for distinction of brain tumors," *Neurology*, vol. 66, no. 12, pp. 1899–1906, 2006.
- [15] J. C. Gore, "Principles and practice of functional mri of the human brain," *J Clin Invest*, vol. 112, no. 1, pp. 4–9, 7 2003.
- [16] R. A. Poldrack, J. A. Mumford, and T. E. Nichols, *Handbook of Functional MRI Data Analysis*, CUP, Cambridge, UK, 2011.
- [17] J. S. Hankins, M. B. McCarville, R. B. Loeffler, M. P. Smeltzer, M. Onciu, F. A. Hoffer, C.-S. Li, W. C. Wang, R. E. Ware, and C. M. Hillenbrand, "R2\* magnetic resonance imaging of the liver in patients with iron overload," *Blood*, vol. 113, no. 20, pp. 4853–4855, 05 2009.
- [18] A. A. Di Tucci, G. Matta, S. Deplano, A. Gabbas, C. Depau, D. Derudas, G. Caocci, A. Agus, and E. Angelucci, "Myocardial iron overload assessment by t2\* magnetic resonance imaging in adult transfusion dependent patients with acquired anemias," *Haematologica*, vol. 93, no. 9, pp. 1385–1388, 2008.
- [19] D. Aquino, A. Bizzi, M. Grisoli, B. Garavaglia, M. G. Bruzzone, N. Nardocci, M. Savoardo, and L. Chiapparini, "Age-related iron deposition in the basal ganglia: Quantitative analysis in healthy subjects," *Radiology*, vol. 252, no. 1, pp. 165–172, 2009, PMID: 19561255.
- [20] M. Callaghan, P. Freund, B. Draganski, E. Anderson, M. Cappelletti, R. Chowdhury, J. Diedrichsen, T. FitzGerald, P. Smittenaar, G. Helms, A. Lutti, and N. Weiskopf, "Widespread age-related differences in the human brain microstructure revealed by quantitative magnetic resonance imaging," *Neurobiology of aging*, vol. 35, pp. 85–96, 02 2014.
- [21] J. M. O'Callaghan, H. E. Holmes, N. M. Powell, J. A. Wells, O. Ismail, I. F. Harrison, B. Siow, R. A. Johnson, Z. Ahmed, A. Fisher, S. Meftah, M. J. O'Neill, T. K. Murray, E. C. Collins, K. Shmueli, and M. F. Lythgoe, "Tissue magnetic susceptibility mapping as a marker of tau pathology in alzheimer's disease," *Neuroimage*, vol. 159, pp. 334 – 345, 2017.
- [22] W. Henneman, J. Sluimer, J. Barnes, W. Flier, I. Sluimer, N. Fox, P. Scheltens, H. Vrenken, and F. Barkhof, "Hippocampal atrophy rates in alzheimer disease: Added value over whole brain volume measures," *Neurology*, vol. 72, pp. 999–1007, 04 2009.
- [23] C. Langkammer, N. Krebs, W. Goessler, E. Scheurer, F. Ebner, K. Yen, F. Fazekas, and S. Ropele, "Quantitative mr imaging of brain iron: A postmortem validation study," *Radiology*, vol. 257, no. 2, pp. 455–462, 2010.
- [24] J. Y. Wang, Q. Q. Zhuang, L. B. Zhu, H. Zhu, T. Li, R. Li, S. F. Chen, C. P. Huang, X. Zhang, and J. H. Zhu, "Meta-analysis of brain iron levels of parkinsons disease patients determined by postmortem and mri measurements," *Scientific Reports*, vol. 6, no. 36669, 2016.
- [25] C. B. Sirlin and S. B. Reeder, "Magnetic resonance imaging quantification of liver iron," *Magnetic resonance imaging clinics of North America*, vol. 18, no. 3, pp. 358–381, 2010.
- [26] D. Hernando, Y. S. Levin, C. B. Sirlin, and S. B. Reeder, "Quantification of liver iron with mri: State of the art and remaining challenges," *J. Magn. Reson. Imaging*, vol. 40, no. 5, pp. 1003–1021, 2014.
- [27] D. L. Donoho, "Compressed sensing," *IEEE Trans. on Information Theory*, vol. 52, no. 4, pp. 1289–1306, 2006.
- [28] E. J. Candès and M. B. Wakin, "An introduction to compressive sampling," *IEEE Signal Process. Mag.*, vol. 25, no. 2, pp. 21–30, 2008.
- [29] S. Boyd, N. Parikh, E. Chu, B. Peleato, and J. Eckstein, "Distributed optimization and statistical learning via the alternating direction method of multipliers," *Found. Trends Mach. Learn.*, vol. 3, no. 1, pp. 1122, Jan. 2011.
- [30] Y. Wang, W. Yin, and J. Zeng, "Global convergence of admm in nonconvex nonsmooth optimization," *J Sci Comput.*, vol. 78, pp. 29–63, 01 2019.
- [31] I. Daubechies, *Ten lectures on wavelets*, Society for Industrial and Applied Mathematics, Philadelphia, PA, USA, 1992.
- [32] D. Dunbar and G. Humphreys, "A spatial data structure for fast poisson-disk sample generation," *ACM Trans. Graph.*, vol. 25, no. 3, pp. 503508, July 2006.
- [33] R. Bridson, "Fast poisson disk sampling in arbitrary dimensions," in *ACM SIGGRAPH 2007 Sketches*, New York, NY, USA, 2007, SIGGRAPH 07, p. 22es, Association for Computing Machinery.
- [34] A. Deshmane, V. Gulani, M. A. Griswold, and N. Seiberlich, "Parallel mr imaging," *J. Magn. Reson. Imaging*, vol. 36, no. 1, pp. 55–72, 2012.
- [35] K. P. Pruessmann, M. Weiger, M. B. Scheidegger, and P. Boesiger, "Sense: Sensitivity encoding for fast mri," *Magn. Reson. Med.*, vol. 42, no. 5, pp. 952–962, 1999.
- [36] M. A. Griswold, P. M. Jakob, R. M. Heidemann, M. Nittka, V. Jellus, J. Wang, B. Kiefer, and A. Haase, "Generalized autocalibrating partially parallel acquisitions (grappa)," *Magn. Reson. Med.*, vol. 47, no. 6, pp. 1202–1210, 2002.
- [37] H. K. Song and L. Dougherty, "k-space weighted image contrast (kwic) for contrast manipulation in projection reconstruction mri," *Magn. Reson. Med.*, vol. 44, no. 6, pp. 825–832, 2000.
- [38] M. I. Altbach, A. Bilgin, Z. Li, E. W. Clarkson, T. P. Trouard, and A. F. Gmitro, "Processing of radial fast spin-echo data for obtaining t2 estimates from a single k-space data set," *Magn. Reson. Med.*, vol. 54, no. 3, pp. 549–559, 2005.
- [39] K. T. Block, M. Uecker, and J. Frahm, "Model-based iterative reconstruction for radial fast spin-echo mri," *IEEE Transactions on Medical Imaging*, vol. 28, no. 11, pp. 1759–1769, 2009.
- [40] T. J. Sumpf, M. Uecker, S. Boretius, and J. Frahm, "Model-based nonlinear inverse reconstruction for t2 mapping using highly undersampled spin-echo mri," *J. Magn. Reson. Imaging*, vol. 34, no. 2, pp. 420–428, 2011.
- [41] C. Huang, C. G. Graff, E. W. Clarkson, A. Bilgin, and M. I. Altbach, "T2 mapping from highly undersampled data by reconstruction of principal component coefficient maps using compressed sensing," *Magn. Reson. Med.*, vol. 67, no. 5, pp. 1355–1366, 2012.
- [42] N. R. Ghugre, C. M. Enriquez, T. D. Coates, M. D. Nelson Jr., and J. C. Wood, "Improved r2\* measurements in myocardial iron overload," *J. Magn. Reson. Imaging*, vol. 23, no. 1, pp. 9–16, 2006.
- [43] T. He, P. D. Gatehouse, G. C. Smith, R. H. Mohiaddin, D. J. Pennell, and D. N. Firmin, "Myocardial t2 measurements in iron-overloaded thalassemia: An in vivo study to investigate optimal methods of quantification," *Magn. Reson. Med.*, vol. 60, no. 5, pp. 1082–1089, 2008.
- [44] T. He, J. Zhang, J.-P. Carpenter, Y. Feng, G. C. Smith, D. J. Pennell, and D. N. Firmin, "Automated truncation method for myocardial t2\* measurement in thalassemia," *J. Magn. Reson. Imaging*, vol. 37, no. 2, pp. 479–483, 2013.
- [45] P. Triadyaksa, M. Oudkerk, and P. E. Sijens, "Cardiac t2\* mapping: Techniques and clinical applications," *J. Magn. Reson. Imaging*, 2019.
- [46] M. Uecker, P. Lai, M. J. Murphy, P. Virtue, M. Elad, J. M. Pauly, S. S. Vasanawala, and M. Lustig, "Espiritan eigenvalue approach to autocalibrating parallel mri: Where sense meets grappa," *Magn. Reson. Med.*, vol. 71, no. 3, pp. 990–1001, 2014.
- [47] R. Fraile and E. García-Ortega, "Fitting an exponential distribution," *Journal of Applied Meteorology*, vol. 44, pp. 1620–1625, 10 2005.
- [48] B. Zhao, W. Lu, T. K. Hitchens, F. Lam, C. Ho, and Z.-P. Liang, "Accelerated mr parameter mapping with low-rank and sparsity constraints," *Magn. Reson. Med.*, vol. 74, no. 2, pp. 489–498, 2015.
- [49] R. E. Carrillo, J. D. McEwen, D. V. D. Ville, J. P. Thiran, and Y. Wiaux, "Sparsity averaging for compressive imaging," *IEEE Signal Processing Letters*, vol. 20, no. 6, pp. 591–594, June 2013.
- [50] A. Beck and M. Teboulle, "A fast iterative shrinkage-thresholding algorithm for linear inverse problems," *SIAM Journal on Imaging Sciences*, vol. 2, no. 1, pp. 183–202, 2009.
- [51] N. Parikh and S. Boyd, "Proximal algorithms," *Foundations and Trends in Optimization*, vol. 1, no. 3, pp. 123–231, 2013.
- [52] Y. Xu, W. Yin, Z. Wen, and Y. Zhang, "An alternating direction algorithm for matrix completion with nonnegative factors," *Computing Research Repository - CORR*, vol. 7, pp. 365384, 03 2012.
- [53] Y. Shen, X. Wen, and Y. Zhang, "Augmented lagrangian alternating direction method for matrix separation based on low-rank factorization," *Optimization Methods and Software*, vol. 29, no. 2, pp. 239–263, 2014.
- [54] Z. Wen, C. Yang, X. Liu, and S. Marchesini, "Alternating direction methods for classical and ptychographic phase retrieval," *Inverse Problems*, vol. 28, no. 11, pp. 115.010, oct 2012.
- [55] R. Lai and S. Osher, "A splitting method for orthogonality constrained problems," *J Sci Comput.*, vol. 58, pp. 431449, 02 2014.
- [56] S. H. Chan, X. Wang, and O. A. Elgendy, "Plug-and-play admm for image restoration: Fixed-point convergence and applications," *IEEE Transactions on Computational Imaging*, vol. 3, no. 1, pp. 84–98, 2017.
- [57] G. Li and T. K. Pong, "Global convergence of splitting methods for nonconvex composite optimization," *SIAM J. Optim.*, vol. 25, no. 4, pp. 2434–2460, 2015.
- [58] M. Hong, Z.-Q. Luo, and M. Razaviyayn, "Convergence analysis of alternating direction method of multipliers for a family of nonconvex problems," *SIAM J. Optim.*, vol. 26, no. 1, pp. 337–364, 2016.